Density of Vibrational States of the Light-Harvesting Complex II of Green Plants Studied by Inelastic Neutron Scattering†

J. Pieper,*,‡ K.-D. Irrgang,*,§ G. Renger,§ and R. E. Lechner‡

Hahn-Meitner-Institut Berlin, Glienicker Str. 100, 14109 Berlin, Germany, and Max-Volmer-Laboratories for Biophysical Chemistry, Technical University, Strasse des 17. Juni 135, 10623 Berlin, Germany

Received: February 13, 2004; In Final Form: April 22, 2004

Results of inelastic neutron scattering (INS) experiments are reported for the solubilized trimeric light-harvesting complex of photosystem II (LHC II) in the temperature range from 5 to 100 K. Two incident neutron wavelengths of 2.0 (∼20 meV) and 5.1 Å (∼3.2 meV) corresponding to elastic energy resolutions of $\Delta E =$ 0.920 meV and $\Delta E =$ 0.093 meV, respectively, are employed to study INS spectra of LHC II for both neutron energy loss and gain. Solubilized LHC II and D_2O-containing buffer solution are investigated separately in order to properly subtract the contribution of the solvent. The inelastic part of the scattering function $S(Q,\omega)$ derived for the LHC II protein resembles the well-known "Boson-peak" and is characterized by a maximum at about 2.5 meV and a strongly asymmetric line shape with a slight tailing toward higher energy transfers. Analysis of the momentum transfer dependence of $S(Q,\omega)$ reveals that both the elastic and inelastic contributions to $S(Q,\omega)$ exhibit the characteristics of vibrational protein motions. Furthermore, the effective density of vibrational states is derived from the experimental data. Finally, the data are discussed in comparison to recent results of line-narrowing optical spectroscopies (Pieper, J.; et al. *J. Phys. Chem. B* **2001**, *105*, 7115). The wide distribution of vibrational frequencies found for LHC II is interpreted in terms of structurally inequivalent protein domains within the LHC II trimer leading to a partial localization of protein phonons.

1. Introduction

Photosynthesis is a fundamental physiological process in nature representing the transformation of solar radiation into storable chemical energy. The photosynthetic apparatus of all oxygen-evolving photoautotrophic organisms such as cyanobacteria, algae, and green plants generally consists of two types of highly specialized pigment−protein complexes referred to as "antennae" and "reaction centers", respectively. During the primary steps of photosynthesis antenna complexes exert a triple function comprising (i) a significant increase of the spatial and spectral absorption cross section of the photosynthetic apparatus, (ii) efficient excitation energy transfer (EET) to photoactive pigments bound in the "reaction center" complexes, and (iii) a regulatory function to protect plants under light stress (for reviews see van Grondelle et al.[1] and Renger[2]).

The major antenna complex of green plants is the light-harvesting complex of photosystem II (LHC II), which binds more than 65% of the total chlorophyll associated with photosystem II (for a review see Paulsen[3]). Its structure has been analyzed by electron crystallography to a resolution of 3.4 Å.[4] The LHC II complex forms a trimer of subunits, which is also assumed to be the dominant form in vivo. Each monomeric subunit contains 12−13 Chl molecules arranged in two layers close to the upper and lower surfaces of the thylakoid membrane and at least two carotenoid molecules. The characteristic features of the protein matrix are three membrane spanning α-helices and a fourth amphipathic helix located at the lumenal side of the thylakoid membrane. However, the present structural resolution does not permit an unambiguous identification of Chl *a* and Chl *b* molecules. So far, the identities of five Chl molecules (Chl *a*1, *a*2, *a*3, *b*5, and *b*6) could be confirmed by spectroscopic studies of LHC II-mutants lacking single pigments, whereas the tentatively assigned Chl *b*3 was found to be a Chl *a*.[5] Another possibility is that both types of pigments can be bound at this site.[6,7]

Time-resolved spectroscopic studies reveal that Chl *b* → Chl *a* excitation energy transfer (EET) in LHC II is ultrafast with kinetic components in the femtosecond−picosecond range and exhibits only a weak temperature dependence.[8−12] A detailed understanding of this rapid dynamics requires information on the energy level structure of the excited electronic states, which is governed by pigment−pigment and pigment−protein interactions.[13−15] Furthermore, the coupling of the purely electronic transitions of pigments to low-frequency vibrational modes of the protein matrix, also referred to as electron−phonon[16] coupling, plays an essential role in light absorption and ultrafast EET (for a review see Kühn et al.[17]).

So far, electron−phonon coupling in antenna complexes has been primarily studied by optical spectroscopy at low temperatures, i.e., spectral hole burning (HB) and fluorescence line-narrowing (FLN) (for reviews see Reddy et al.[18] and Jankowiak et al.[19,20]). HB utilizes quasi-monochromatic laser light to selectively bleach a particular transition frequency within an inhomogeneously broadened absorption band. As a result, HB induces a change in the absorption spectrum, which typically appears as a "hole" at the burn frequency. Analysis of electron−phonon coupling is mainly based on the observation of satellite holes beside the burn frequency, i.e., the so-called phonon sideband holes. The shape of the overall HB spectrum is determined by the Huang−Rhys factor S, which represents the electron−phonon coupling strength, and the one-phonon profile that is related to the density of vibrational states.[21,22,23] FLN is

† Part of the special issue "Gerald Small Festschrift".

* To whom correspondence should be addressed. E-mail: pieper@hmi.de (J.P.); irrg0532@mailbox.tu-berlin.de (K.-D.I.; sample preparation and biochemical analysis).

‡ Hahn-Meitner-Institut Berlin.

§ Technical University.

10.1021/jp049341f CCC: $27.50 © 2004 American Chemical Society
Published on Web 06/12/2004

a technique complementary to HB where emission is selectively excited at a certain transition frequency within an inhomogeneously broadened fluorescence band. Within the limits of linear Franck−Condon (electron−phonon) coupling, homogeneously broadened absorption and fluorescence spectra should exhibit mirror symmetry.[24]

Because of the short lifetime of excited electronic states in systems with efficient EET, analysis of electron−phonon coupling by line-narrowing spectroscopy (HB and FLN) is often restricted to investigations of the lowest excited electronic state(s). In the case of LHC II, a relatively weak transition at ∼680 nm was first assigned as the lowest and fluorescing Q_y state based on hole burning spectroscopy at 4.2 K[25] and pump−probe experiments at room temperature.[26,27] Subsequently, reabsorption studies[13] as well as fluorescence line-narrowing and temperature-dependent absorption experiments[28] confirmed the existence of a 680 nm state. More detailed hole burning experiments[29] revealed the presence of a complex low-energy level structure with three Q_y states located at (677.1 ± 0.2), (678.4 ± 0.2), and (679.8 ± 0.2) nm and having inhomogeneous widths of their absorption bands of (80 ± 10) cm^{-1}. The combined absorption intensity of these states is equivalent to that of three Chl *a* molecules per LHC II trimer. Therefore, it appears reasonable to assume that each state is highly localized on one Chl *a* molecule of a subunit. The latter assignment of low-energy Q_y states is in line with recent results of single molecule spectroscopy on trimeric LHC II typically showing three emission lines in the vicinity of 680 nm, which are separated by 20−100 cm^{-1}.[30] Furthermore, it is in qualitative agreement with the recently reported structural heterogeneity of trimeric LHC II.[31,32,33]

Information on the electron−phonon coupling for trimeric LHC II was gathered from 4.2 K hole burning[25,29] and fluorescence line-narrowing experiments.[28,34] Spectral hole burning[29] led to the conclusion that the lowest Q_y state of this complex is characterized by weak electron−phonon coupling to a one-phonon profile with a mean phonon frequency of $\omega_m = 18$ cm^{-1}, a width of ∼ 25 cm^{-1} and $S = 0.8$. Inspection of line-narrowed fluorescence spectra[28,34] yielded mean phonon frequencies ω_m of 22−24 cm^{-1} and a strongly asymmetric one-phonon profile with a width of ∼65 cm^{-1}. Because the zero-phonon line is typically contaminated with scattered laser light in FLN spectra, the *S* factor could not directly be obtained. In ref 28, a value of ∼0.6 was determined by fitting the low-energy wing of temperature-dependent absorption spectra of LHC II using the latter one-phonon profile and assuming that the lowest state is located at 676 nm. Weak electron−phonon coupling with $S < 1$ and ω_m values of 20−30 cm^{-1} are typically observed for photosynthetic antenna complexes (for a review see, e.g., Reddy et al.[18]). Nevertheless, the shapes of the one-phonon profile reported for LHC II in the above studies differ significantly. Therefore, our FLN[34] and HB[29] results were simultaneously analyzed using a model that is able to account for the phonon structure of both types of line-narrowed spectra.[34,35] The simulations revealed that the lowest Q_y state of LHC II at ∼680.0 nm is characterized by weak electron−phonon coupling with a Huang−Rhys factor of ∼ 0.9 to a broad and strongly asymmetric one-phonon profile with a peak frequency ω_m of 15 cm^{-1} and a width of $\Gamma = 105$ cm^{-1}. It could be shown that the obviously different shapes of the phonon structure in HB and FLN measurements arise from a breakdown of mirror symmetry between the real- and pseudo-phonon sideband contributions. This situation can be anticipated, when the width of the one-phonon profile ($\Gamma = 105$ cm^{-1}) becomes comparable or broader than the inhomogeneous width ($\Gamma_{inh} = 80$ cm^{-1}) as in the case of LHC II.[35] A similar situation has recently been reported for the LH2 antenna complex of purple bacteria.[36]

The above-described inherent complexity in interpretation of phonon structure in HB and FLN spectra requires the application of an independent experimental approach to study the vibrational density of states of photosynthetic pigment−protein complexes. Thus, inelastic neutron scattering (INS) becomes the technique of choice for further studies on LHC II. Because of the high incoherent scattering cross section of hydrogen atoms, which are almost homogeneously distributed in biomolecules, INS is widely used to study diffusive[37] as well as vibrational dynamics of proteins.[38] Focusing on the latter aspect, INS spectra of proteins generally display a peak centered at energy transfers of 2−5 meV representing an excess of vibrational modes compared to the Debye-like density of states. The origin of this so-called "Boson peak", known to be characteristic for both proteins and glassy systems,[39−44] is not yet fully clarified. However, it is widely accepted that it is related to the disordered nature of these systems. Furthermore, the effective density of states can be derived from INS spectra (see, e.g., refs 39 and 42), which permits comparison to molecular dynamics (MD) simulations of internal protein motions (see, e.g., Paciaroni et al.[45]).

In the present contribution, we report results of INS experiments for the photosynthetic antenna complex LHC II from spinach. A special preparation protocol was developed which ensured that trimeric LHC II was properly solubilized in a D_2O containing buffer solution and that the solvent scattering was significantly reduced. To study INS spectra of LHC II for both neutron energy loss and gain as well as for two different elastic energy resolutions, two incident neutron wavelengths of 2.0 (∼20 meV) and 5.1 Å (∼3.2 meV) are employed. The momentum transfer and temperature dependencies of $S(Q,\omega)$ are analyzed to prove the vibrational nature of the protein motions under study. Furthermore, the effective density of vibrational states is derived from the experimental data. Finally, the data are discussed in comparison to recent results of line-narrowing optical spectroscopy.[34,35] A possible origin of the wide distribution of vibrational modes is discussed in terms of the LHC II structure.

2. Materials and Methods

Sample Preparation. LHC II was purified from spinach photosystem II membrane fragments by sucrose density gradient centrifugation in the presence of *n*-*β*-dodecylmaltoside as described previously.[46] This trimeric LHC II was shown to be phosphorylated on Threonine (Thr) residues by using anti P−Thr (Zymed) in Western blotting experiments (data not shown). The protein composition of LHC II was analyzed by SDS/urea/PAGE at 4°C in combination with silver staining as reported earlier.[47,48] Samples equivalent to 5 μg Chl were loaded onto the gels. Furthermore, Lhcb 1, 2, 3, 5, 6 antibodies directed against synthetic peptides derived from the primary structures of the mature forms of the various LHC II apoproteins (Agrisera, Sweden), monoclonal anti Lhcb4, polyclonal anti PsbS, and anti PsbA were used to analyze the protein composition of the large scale preparations in detail by immunoblotting. No PsbA and Lhcb4 were identified, PsbS contributed less than 1% and Lhcb 5/6 less than 5% to the total amount of protein as semiquantitatively analyzed by densitometric scanning of the immunodecorated bands on polyvinylidene fluoride membranes. Chl concentrations were determined as recommended by Porra et

al.[49] The carotenoid content as well as the Chl/carotenoid ratio was calculated from measurements of the sample absorptions at 470, 646, 663, and 750 nm in 80% v/v acetone according to Porra et al.[49] and Wellburn & Lichtenthaler.[50] The Chl a/b ratio (w/w) was determined to be 1.36 ± 0.6 ($n = 22$). The protein content of LHC II samples was routinely analyzed following the method of Brown et al.[51] The molecular weight determined by gel filtration column chromatography (Superose HR 10/30, Amersham Biotech) in combination with a FPLC system, density gradient centrifugation or analytical ultracentrifugation was 175 ± 20 kDa for the holocomplex including Chl *a*/*b*, carotenoids, and the *n*-β-dodecylmaltoside shell surrounding the pigment−protein complex. This mass is only compatible with the trimeric form of LHC II. At the employed detergent concentration of 0.025% w/v *n*-β-dodecylmaltoside the trimeric form is highly stable and can, therefore, safely be presumed as the form of LHC II under investigation in the present INS study. Absorption spectra were recorded in the range of 350−800 nm before and after concentrating the samples using a Beckman spectrophotometer (DU-64). The Q_y-absorption spectrum at room temperature exhibited two bands with maxima at 652 ± 1 and 675 ± 1 nm.

Up to 12 different LHC II preparations were pooled and concentrated in Ultrafree 50 tubes (Millipore) with an exclusion size of 50 kDa using a Heraeus labofuge 400 R. This procedure yielded a final amount of 25−30 mg Chl per neutron scattering experiment. The latter value is equivalent to a total protein mass of approximately 100−120 mg. Samples were always handled under dim green light. The concentrated pigment−protein-complexes were dropped into liquid nitrogen and the frozen globules lyophilised in the dark to remove H_2O. Lyophilised samples were finally resuspended in D_2O (99.9% D, Eurisotop, CEA group, Saclay, France) yielding a concentration of about 25 mg Chl/mL. In detail, the buffer solution contained 25 mM Mes-NaOD, 10 mM $CaCl_2$, 0.025% w/v β-dodecylmaltoside, and 30% w/v sucrose. The pD-value was adjusted to 6.7 by adding NaOD. The above-described analysis of the protein composition by SDS/urea/PAGE, absorption spectroscopy, and pigment determination was repeated after each neutron scattering experiment, but no significant modifications due to radiation damage could be observed (see silver stained gel in Figure 1).

INS Measurements. INS experiments were performed using the time-of-flight spectrometer NEAT[52,53,54] (BENSC, Hahn-Meitner Institute, Berlin-Germany). INS spectra were recorded using incident neutron wavelengths of 2.0 (∼20 meV) and 5.1 Å (∼3.2 meV) corresponding to (elastic) Q ranges of 1.0−5.7 $Å^{-1}$ and 0.3−2.3 $Å^{-1}$, respectively. The elastic energy resolutions were $\Delta E = 0.920$ meV and $\Delta E = 0.093$ meV, respectively. The samples were transferred into cylindrical aluminum cells having an effective volume of 1.2 mL. Solubilized LHC II complexes and the D_2O-containing buffer solution were studied separately in order to independently investigate the contribution of the solvent. The elastic resolution was determined by vanadium standard runs. In INS experiments, however, the resolution is a function of energy transfer. The energy transfer dependence of the resolution has been calculated according to Lechner[55] based on the experimentally obtained elastic resolution width.

The INS data were corrected for detector efficiency and sample-geometry dependent attenuation, normalized, as well as transferred to energy scale using the program package FITMO-3.

The sample temperature was maintained using an Orange Cryofurnace and stabilized by a Lakeshore temperature controller. Prior to neutron scattering measurements the temperature was allowed to equilibrate for 30 min.

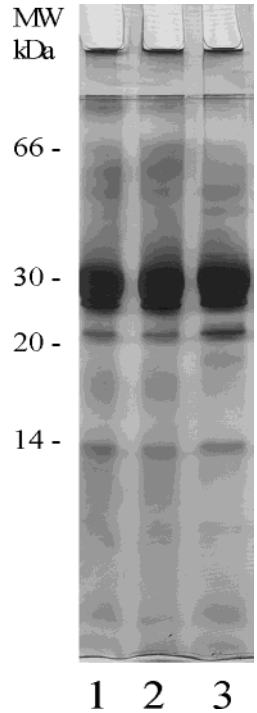

Figure 1. SDS/urea/PAGE of LHC II preparations obtained after neutron scattering experiments (lanes 1 and 2) in comparison to a dissolved lyophilised sample prior to a neutron scattering experiment (lane 3). Molecular weights have been determined using marker proteins (Amersham Bioscience, Freiburg).

Throughout the paper the term "energy transfer" denotes the energy transferred between neutron and sample which is a general convention in neutron scattering. It should not be mixed with "excitation energy transfer" (EET), i.e., the transfer of light-induced electronic excitations within photosynthetic antennae and to reaction center complexes. All energy transfer values are given in meV, whereas vibrational energies in line-narrowed optical spectra are reported in wavenumbers (cm^{-1}). Here, 1 meV = 8.006 cm^{-1}.

Theoretical Background. To compare results from optical and neutron scattering experiments, the principles of phonon spectroscopy by INS, HB, and FLN shall be briefly summarized.

In an INS experiment, the measured quantity is the incoherent scattering function $S(Q,\omega)$, where Q is the momentum and ω the energy transferred to the scattered neutron. Since our experiments are limited to low temperatures ($T \leq 100$ K) and to large or medium energy resolution widths ($\Delta E \geq 90$ μeV), quasielastic scattering is absent and inelastic neutron scattering will be due to vibrational excitations only. In our description, we will, for practical reasons, use expressions developed for phonon propagation in long-range ordered crystalline systems. It is clear that proteins do not present this type of order, and therefore, the spatial propagation of vibrational modes will be restricted to shorter ranges. Nevertheless, in the absence of an exact theory, we expect this to be a good approximation and employ a phonon expansion to extract an effective vibrational density of states from the measured data. Within this approach, the neutron scattering function, $S(Q,\omega)$, is given by[56]

$$S(Q,\omega) = e^{-\langle u^2\rangle Q^2}\left\{\delta(\omega) + \left(\frac{\langle u^2\rangle Q^2}{1!}\right)S_1(\omega) + \left(\frac{[\langle u^2\rangle Q^2]^2}{2!}\right)S_2(\omega) + \ldots + \left(\frac{[\langle u^2\rangle Q^2]^R}{R!}\right)S_R(\omega) + \ldots\right\} \quad (1)$$

with $\langle u^2\rangle$ being the average atomic mean square displacement.

Here, the first term $\delta(\omega)$ represents the purely elastic scattering, whereas the $S_R(\omega)$ terms correspond to R-phonon transitions ($R = 1, 2, ...$). The normalized one-phonon term $S_1(\omega)$ is given by

$$S_1(\omega) = [2\omega \sinh(\hbar\omega/2kT)]^{-1} \exp(-\hbar\omega/2kT)g(\omega) \quad (2)$$

where T is the temperature, k and $\hbar$ are the Boltzmann and Planck constants, respectively. The term $g(\omega)$ has to be considered as an effective density of states accounting for the individual Debye−Waller factor, phonon polarization vector, and reciprocal mass of each generalized oscillator of the complex protein system. Each profile S_R ($R > 1$) is obtained by folding S_1 with itself R times. Employing a one-phonon approximation, which is valid for the typically small values of $\langle u^2\rangle$ and Q^2 (see ref 57, page 52), eq 1 reduces to

$$S(Q,\omega) = e^{-\langle u^2\rangle Q^2}\{\delta(\omega) + \langle u^2\rangle Q^2 S_1(\omega)\} \quad (3)$$

where $e^{-\langle u^2\rangle Q^2}$ is the Debye−Waller factor. In the present paper, the values of $\langle u^2\rangle$ and Q^2 are in the order of 10^{-2}−10^{-3} Å^2 and 10^{-1}−10^{1} Å^{-2}, respectively. Thus, for the highest values of both, $\langle u^2\rangle$ and Q^2, two-phonon contributions will represent less than 5% of the one-phonon part in the scattered intensity, as can easily be seen by inspecting the pre-factors of the one- and two-phonon terms in eq 1. Therefore, the application of the one-phonon approximation is justified.

INS spectra are measured at constant scattering angles Φ, so that the momentum transfer Q varies with energy transfer following

$$Q^2(\omega,\Phi) = \frac{8\Pi^2}{\lambda_0^{\,2}}\left\{1 + \frac{\hbar\omega}{2E_0} - \sqrt{1 + \frac{\hbar\omega}{E_0}}\cos\Phi\right\} \quad (4)$$

where λ_0 and E_0 are the wavelength and energy of the incident neutrons, respectively. Finally, when simulating experimental INS spectra, $S(Q,\omega)$ as given by eq 3 has to be folded with the resolution function derived from a vanadium standard run.

In optical spectroscopy of amorphous systems such as pigment−protein-complexes, two main differences have to be taken into account compared to the theory of INS described above: (i) the term $\langle u^2\rangle Q^2$ is replaced by the Huang−Rhys factor S reflecting the coupling strength of an electronic transition to a distribution of delocalized phonons and (ii) due to structural heterogeneity the electronic transitions of an ensemble of pigments are distributed according to an inhomogeneous distribution function $N(\Omega_0 - \omega_C)$ having a peak position of ω_C and a width of Γ_{inh}. Within the linear, harmonic Franck−Condon approximation the absorption spectrum $A(\omega)$ of a pigment−protein complex in the low-temperature limit is given by[21]

$$A(\omega) = \sum_{R=0}^{\infty}\left(S^R\frac{e^{-S}}{R!}\right)\int d\Omega_0\, N(\Omega_0 - \omega_C) l_R(\omega - \Omega_0 - R\omega_m) \quad (5)$$

The normalized line shape $l_0(\omega - \Omega_0)$ denotes the zero-phonon line (ZPL) representing the purely electronic transition with a peak position of Ω_0 and a width of γ. The phonon sideband (PSB) comprises all R-phonon transitions ($R = 1, 2, ...$) with normalized line shapes $l_R(\omega - \Omega_0 - R\omega_m)$ having a peak position of $\Omega_0 + R\omega_m$ for a mean phonon frequency of ω_m. The one-phonon profile $l_1(\omega - \Omega_0 - \omega_m)$ is different from $S_1(\omega)$ discussed above and represents the product $g(\omega)D(\omega)$ with $g(\omega)$ being the density of states of the phonon modes and $D(\omega)$ an electron−phonon coupling term. Therefore, it is sometimes also called "weighted density of states". Note that this expression of $l_1(\omega - \Omega_0 - \omega_m)$ is furthermore based on a mean frequency approximation.[21] In agreement with experimental data,[21,29,34] l_1 is assumed to be asymmetric with a Gaussian and a Lorentzian profile as its low- and high-energy wing, respectively. Thus, the full profile l_1 has a peak frequency of ω_m and a width of $\Gamma = \Gamma_{Gauss}/2 + \Gamma_{Lorentz}/2$. Each profile l_R ($R > 1$) is obtained by folding l_1 with itself R times.

The spectral resolution can be substantially improved using line-narrowing techniques such as HB and FLN. In the low-temperature and short burn time limits, the "hole-burned" spectrum $\Delta A(\omega)$ for a burn frequency ω_B is given by[21]

$$\Delta A(\omega) = \sum_{R,P=0}^{\infty} S^R\frac{e^{-S}}{R!}S^P\frac{e^{-S}}{P!}\int N(\Omega_0 - \omega_C) \times l_R(\omega - \Omega_0 - R\omega_m) l_P(\omega_B - \Omega_0 - P\omega_m)\, d\Omega_0 \quad (6a)$$

Using the approach of Personov,[24] the low-temperature FLN spectrum, $F(\omega)$, is given by eq 6a with l_R replaced by $l_R(\omega - \Omega_0 + R\omega_m)$

$$\Delta A(\omega) = \sum_{R,P=0}^{\infty} S^R\frac{e^{-S}}{R!}S^P\frac{e^{-S}}{P!}\int N(\Omega_0 - \omega_C) \times l_R(\omega - \Omega_0 + R\omega_m) l_P(\omega_B - \Omega_0 - P\omega_m)\, d\Omega_0 \quad (6b)$$

where ω_E is the excitation frequency.

3. Results and Discussion

Low-Temperature INS Spectra of LHC II. INS spectra were first measured with an incident neutron wavelength of 2 Å (~20 meV) at temperatures of 5, 40, and 80 K in order to characterize the vibrational density of states of trimeric LHC II. Low temperatures were chosen in order to ensure the best possible comparability to the 4.2 K line-narrowed optical spectra of refs 29 and 34, low probability of multi-phonon processes, as well as validity of the harmonic approximation for the protein vibrations under investigation. Furthermore, it is well-established that EET in antenna complexes is fully functional for temperatures in the above range (see, e.g., reviews 18 and 20). In the case of LHC II, the time constants for Chl *b* → Chl *a* EET are only weakly temperature dependent. As an example, the fastest EET component is only slowed from ~150 fs at room temperature[8,10] to 310 fs at 12 K.[11]

Due to the relatively high incident energy of ~20 meV, the scattering function $S(Q,\omega)$ can be obtained in an almost symmetric window of energy transfers from −15 to +20 meV, i.e., in neutron energy loss as well as in neutron energy gain, with an elastic resolution of 0.920 meV. Typical 80 K−INS spectra for this setup are shown in Figure 2 for both solubilized LHC II (curve a, upper full line) and the D_2O-containing buffer solution (curve b, dotted line). The latter contribution was normalized in order to reflect the amount of buffer present in solubilized LHC II. In Figure 2, the features on the left-hand side of the elastic peak at 0 meV correspond to neutron energy loss (negative energy transfers), whereas those on the right-hand side represent neutron energy gain (positive energy transfers). On the energy loss side of the neutrons, the spectrum of solubilized LHC II exhibits two distinct features, an intense peak at about 7 meV and a less discernible structure at about −2.5 meV. Inspection of the buffer data reveals that the feature at 7 meV can clearly be attributed to the solvent. Qualitatively similar observations can be made on the energy gain side of the neutrons. However, in the latter case, no distinct peaks are

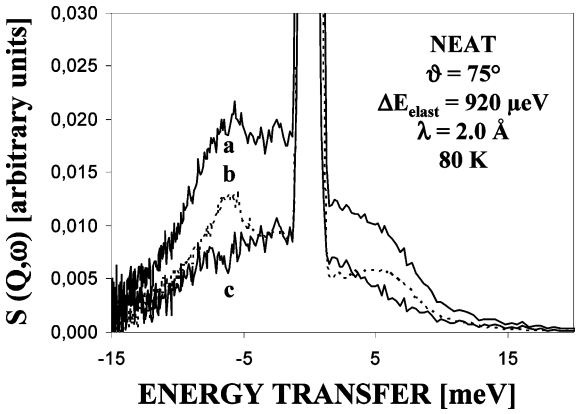

Figure 2. INS spectra of solubilized LHC II (upper full line, curve a) and buffer solution (dashed line, curve b) obtained with an incident neutron wavelength of 2 Å and an elastic resolution of 0.920 meV at 80 K. The lower full line is the difference spectrum attributed to the LHCII complex (curve c).

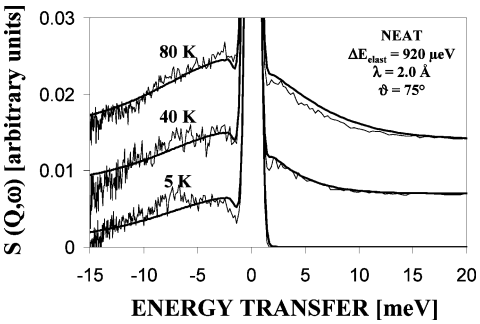

Figure 3. Temperature dependence of INS spectra of LHC II obtained with an incident neutron wavelength of 2 Å and an elastic resolution of 0.920 meV. The spectra are given equidistant offsets of 0.007 for ease of inspection. The smooth, full lines correspond to theoretical fits calculated according to eq 3 (see text for parameters).

observed for solubilized LHC II due to the low thermal occupation of higher-frequency modes at a temperature of 80 K ($kT \sim 7$ meV) and the lower resolution at positive energy transfer values. Nevertheless, it is obvious that the buffer contribution is less pronounced in the low-frequency region at about 2−3 meV. These findings suggest that the vibrational motions of the LHC II protein and its surrounding buffer solution are largely uncoupled. In this case, the difference of curves a and b shown as the lower full line in Figure 2 (curve c) reflects the scattering function $S(Q,\omega)$ for LHC II at a temperature of 80 K. It is remarkable that, in contrast to the spectrum of solubilized LHC II (curve a), curve c is almost symmetric around the elastic peak with a maximum at about ±2−3 meV, a very slight tailing toward higher energy transfers and a somewhat lower intensity at the neutron energy gain side. This is consistent with its maximum at about ± 2−3 meV being at lower energy transfers than kT for 80 K (6.95 meV) and confirms that the buffer contribution was properly subtracted. Finally, data obtained at temperatures of 5 and 40 K were treated the same way (not shown). The resulting scattering functions $S(Q,\omega)$ for LHC II at 5, 40, and 80 K are shown for comparison in Figure 3. The data qualitatively exhibit the expected temperature dependence. For neutron energy loss, the shape of $S(Q,\omega)$ remains almost the same, whereas the integrated inelastic intensity increases with increasing temperature. In contrast to this, the influence of subsequent thermal population of vibrational levels with rising temperature is clearly visible in neutron energy gain. Here, no inelastic contribution is observed at 5 K, whereas the scattering functions $S(Q,\omega)$ exhibits a more

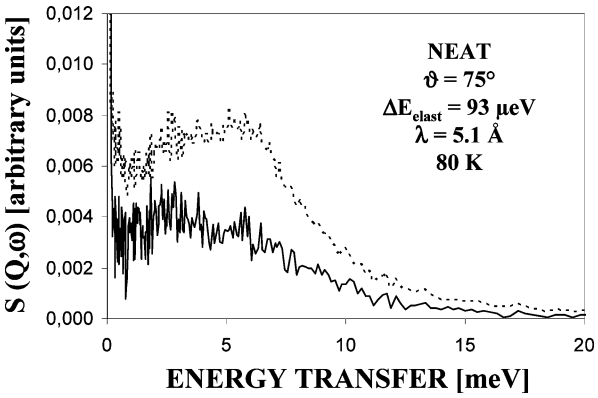

Figure 4. INS spectra of solubilized LHC II (dashed line) and LHCII complex (full line) obtained with an incident neutron wavelength of 5.1 Å and an elastic resolution of 0.093 meV at 80 K.

pronounced mirror symmetry at higher temperatures. Furthermore, the data shown in Figure 3 exhibit a weak additional peak at about 7 meV. However, this feature is coincident with the position of the inelastic peak observed in the buffer spectrum. Thus, it is possible that the weak peak at about 7 meV is not a real feature but rather due to a slight uncertainty in the subtraction procedure described above or in the H−D exchange of the solubilized LHC II sample (the incoherent scattering cross section of H is about 40 times higher than that of D).

Analogous INS experiments were performed using an incident neutron wavelength of 5.1 Å at temperatures of 40, 80, and 100 K. Because of the relatively small incident energy of ∼3.2 meV, the analysis is now restricted to neutron energy gain with energy transfers from −1 to +20 meV. At the same time, the elastic resolution can be significantly increased to 0.093 meV. In addition, due to the higher flux of the cold neutron source at 5.1 Å, the data statistics is considerably improved. A typical INS spectrum obtained with this setup at 80 K is shown in Figure 4 for solubilized LHC II (dotted line). As found for the configuration used above (incident wavelength of 2 Å), the spectrum of solubilized LHC II exhibits two distinct features at ∼2.5 and ∼7 meV. Again, the feature at 7 meV can clearly be attributed to the solvent (not shown), so that the difference spectrum shown as a full line in Figure 4 reflects the scattering function $S(Q,\omega)$ for LHC II at a temperature of 80 K. The latter spectrum exhibits a similar shape as found above, but in contrast to the lower resolution data, a peak at about 2.5 meV becomes clearly discernible from the elastic peak. The data obtained at temperatures of 40 and 100 K were treated in the same way (not shown). The resulting scattering functions $S(Q,\omega)$ for LHC II at 40, 80, and 100 K are shown for comparison in Figure 5. Note that the peak at about 7 meV is virtually absent in these data. This confirms that a peak at this position found in the 2 Å data (see above) might be due to a slight uncertainty in the subtraction of the buffer contribution or in the H−D exchange of the solubilized LHC II sample.

Vibrational Nature of the Inelastic Features. After deriving the scattering functions $S(Q,\omega)$ for LHC II from the experimental data, the nature of the spectral features shall be briefly discussed. In this regard, it is instructive to check as to which extent the elastic as well as the inelastic contributions to $S(Q,\omega)$ follow the behavior predicted by eq 3. The left frame of Figure 6 shows a logarithmic plot of the elastic peak intensity of the 2 Å spectra as a function of Q^2 for three different temperatures. According to eq 3, the data can be well fit by linear functions with slopes which represent the average atomic mean square displacement $\langle u^2 \rangle$ for the LHC II protein at each temperature. Values of 0.006, 0.009, and 0.013 Å^2 can be calculated for temperatures of 5,

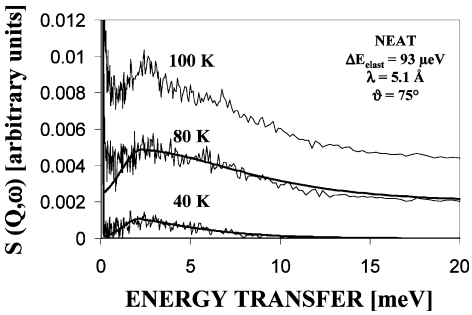

Figure 5. Temperature dependence of INS spectra of LHC II obtained with an incident neutron wavelength of 5.1 Å and an elastic resolution of 0.093 meV. The spectra are given equidistant offsets of 0.002 for ease of inspection. The smooth, full lines correspond to theoretical fits calculated according to eq 3 (see text for parameters).

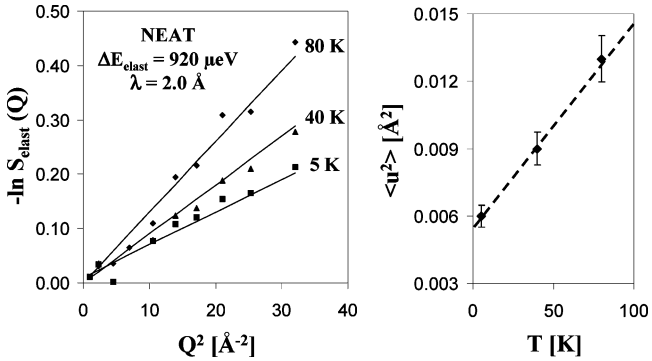

Figure 6. Left: logarithmic plot of the elastic intensity of temperature-dependent INS spectra shown in Figure 4 as a function of the squared momentum transfer Q^2. The data were obtained with an incident neutron wavelength of 2 Å and an elastic resolution of 0.920 meV. The full lines correspond to linear fits according to eq 3. The resulting $\langle u^2 \rangle$ values of 0.006, 0.009, and 0.013 for 5, 40, and 80 K, respectively, are shown on the right together with a linear fit (dashed line) for ease of inspection.

40, and 80 K, respectively; that is, the value of $\langle u^2 \rangle$ increases almost linearly with temperature (see right Frame of Figure 6). The value of $\langle u^2 \rangle$ also determines the Debye−Waller factor at each given Q. A linear increase of $\langle u^2 \rangle$ with temperature is generally predicted for the case of vibrational motions[57] and has already been reported for PS II membrane fragments[58] and the bacterial reaction center.[59] Furthermore, the $\langle u^2 \rangle$ values found for the latter two systems were of the same order of magnitude as determined here for LHC II.

Figure 7 shows the inelastic part of the scattering functions $S(Q,\omega)$ for LHC II at 80 K obtained using an incident neutron wavelength of 2 Å at different scattering angles, i.e., for different momentum transfers Q. It is apparent from these data that the shape of the inelastic contribution with a peak at about −2.5 meV remains virtually invariant, whereas the peak intensity increases with increasing momentum transfer Q. A quantitative illustration of this behavior is given in the inset of Figure 7, where the value of $S(Q,\omega)$ at −2.5 meV divided by the corresponding Debye−Waller factor is shown as a function of Q^2. In good agreement with eq 3, the plotted function increases almost linearly with increasing Q^2, with a slope of $\langle u^2 \rangle S_1(\omega)$. A plot of the inelastic part of the scattering functions $S(Q,\omega)$ for LHC II obtained using an incident neutron wavelength of 5.1 Å at 100 K is shown in Figure 8. In principle, the 5.1 Å data exhibit similar features as discussed above for the other incident neutron wavelength. The peak intensity of the inelastic contribution increases with increasing momentum transfer Q, whereas its shape remains almost unchanged. Furthermore, the peak intensity at 2.5 meV divided by the corresponding Debye−Waller factor increases linearly with increasing Q^2 in line with

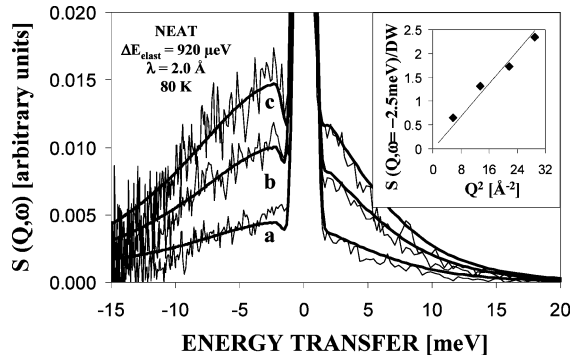

Figure 7. INS spectra of LHC II obtained for different scattering angles with an incident neutron wavelength of 2 Å and an elastic resolution of 0.920 meV at 80 K. The curves a, b, and c correspond to scattering angles of 46, 75, and 125° or Q^2 values (at $\omega = -2.5$ meV) of 5.7, 13.5, and 29.1 Å^2, respectively. The smooth, full lines correspond to theoretical fits calculated according to eq 3 (see text for parameters). The inset shows the inelastic intensity at $\omega = -2.5$ meV divided by the Debye−Waller factor as a function of the squared momentum transfer Q^2 at $\omega = -2.5$ meV. A linear fit is given for ease of inspection.

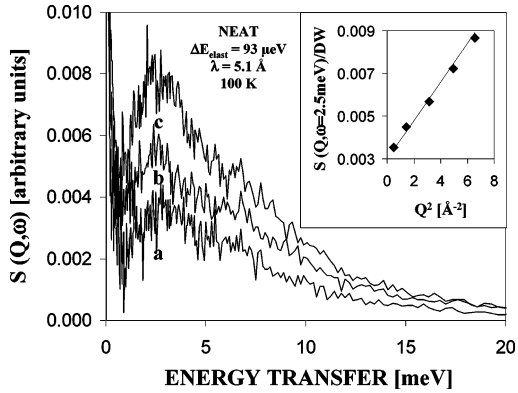

Figure 8. INS spectra of LHC II obtained for different scattering angles with an incident neutron wavelength of 5.1 Å and an elastic resolution of 0.093 meV at 100 K. The curves a, b, and c correspond to scattering angles of 22, 75, and 125° or Q^2 values (at $\omega = 2.5$ meV) of 0.5, 3.1, and 6.57 Å^2, respectively.. The inset shows the inelastic intensity at $\omega = 2.5$ meV divided by the Debye−Waller factor as a function of the squared momentum transfer Q^2 at $\omega = 2.5$ meV. A linear fit is given for ease of inspection.

eq 3 (see inset of Figure 8). In contrast to the situation described above, the linear fit cannot be extrapolated to 0 for $Q^2 = 0$. This might be due to a slight contribution of multiple scattering.

In summary of the results presented above, three important features were found to characterize the dynamics of LHC II at temperatures of 5−100 K: (a) a linear Q^2 dependence of the elastic intensity, (b) a linear Q^2 dependence of the inelastic peak intensity divided by the Debye−Waller factor, and (c) a linear temperature dependence of the average atomic mean square displacement $\langle u^2 \rangle$. Based on these findings, it can be concluded that both the elastic and inelastic contributions of the INS data presented here follow the Q dependence given by eq 3. Thus, the INS data display the signature of harmonic vibrational protein dynamics of LHC II in the investigated temperature range. Furthermore, the above findings indicate that coherent contributions are negligible within experimental error. Since coherent scattering could arise mainly from the D_2O-containg buffer solution, the latter finding also proves the proper subtraction of the solvent contribution.

Vibrational Density of States. It has already been mentioned above that the INS spectra of LHC II resemble the typical "Boson peak" behavior of proteins with a peak centered at about

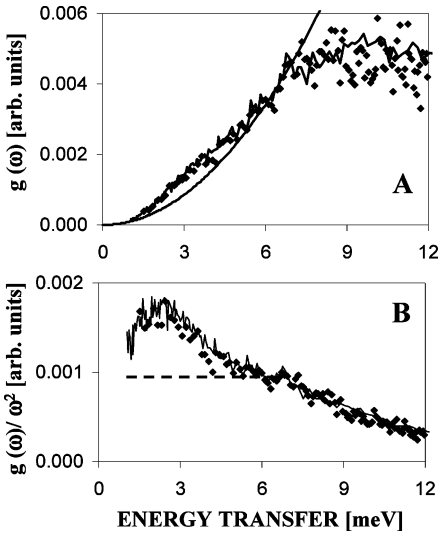

Figure 9. Effective density of states $g(\omega)$ of LHC II (frame A) as well as the $g(\omega)/\omega^2$ representation (frame B) as obtained using an incident neutron wavelength of 2 Å (diamonds) and 5.1 Å (full lines). The smooth full line in frame A is an ω^2 function fitted to the low-energy part of the effective density of states $g(\omega)$ for comparison, to test a possible deviation from a Debye-like density of vibrational states with $g(\omega)$ being proportional to ω^2. It is seen that $g(\omega)$ of LHC II indeed displays an excess of vibrational modes. The plot of the $g(\omega)/\omega^2$ function in frame B is displayed together with the ω^2 curve of frame A, now transformed into a constant, as a dashed horizontal line. This representation makes the excess of vibrational modes extending over a frequency range around 3 ± 2 meV more clearly visible.

2.5 meV and a slight tailing toward higher energy transfers. Then, the effective vibrational density of states $g(\omega)$ of LHC II can be calculated from $S(Q,\omega)$ according to eqs 2 and 3. Determination of $g(\omega)$ was mainly based on the INS data obtained in neutron energy loss for an incident wavelength of 2 Å, because under these conditions the accessible energy transfer range is wider (0−15 meV) and the influence of thermal population effects is smaller in the investigated temperature range. Furthermore, data statistics was improved by grouping over all scattering angles in this case. The Debye−Waller factor at each Q value was calculated based on $\langle u^2 \rangle$ values found by investigating the Q dependence of the elastic peak intensity above. As expected, the resulting $g(\omega)$ was similar for each temperature within experimental error. Thus, results for $g(\omega)$ obtained separately from the 5, 40, and 80 K data (not shown) were averaged to yield the effective density of vibrational states $g(\omega)$ displayed by diamonds in frame A of Figure 9. In a second step $g(\omega)$ was calculated from the data obtained using an incident wavelength of 5.1 Å at 100 K. The result is shown as a full line in Figure 9 and fully confirms $g(\omega)$ calculated from the neutron energy loss side data.

To test a possible deviation from a Debye-like density of vibrational states with $g(\omega)$ being proportional to ω^2, frame A of Figure 9 shows a plot of $g(\omega)$ together with a curve proportional to ω^2, which was fitted to the low-energy part of the experimentally obtained density of states. An inspection of these data reveals that $g(\omega)$ of LHC II indeed displays an excess of vibrational modes. For comparison, a plot of the $g(\omega)/\omega^2$ function is also shown as a full, smooth line in frame B of Figure 9. The ω^2 curve of frame A, now transformed into a constant, is shown as a dashed horizontal line. This representation makes the excess of vibrational modes extending over a frequency range around 3 ± 2 meV more clearly visible. In conclusion, the density of vibrational states $g(\omega)$ of LHC II was determined for energy transfers of 0−12 meV and exhibits properties typical for proteins with an excess of vibrational modes compared to the Debye behavior. This is the reason for observation of the characteristic vibrational peak in its INS spectra at low energy transfers. Similar $g(\omega)$ functions were determined for other proteins such as myoglobin[39] and β-lactoglobulin[42] and seem to generally reflect the disordered nature of protein molecules.

Temperature Dependence. Qualitatively, the temperature dependence of the INS spectra of LHC II shown in Figures 3 and 5 has already been discussed above. To theoretically describe these data, the one-phonon function $S_1(Q,\omega)$ is assumed to be given by a normalized phenomenologic line shape function consisting of a Gaussian and a Lorentzian at the low- and high-energy transfer sides of its maximum, respectively. This approach is similar to that used in description of the optical spectroscopy data (see Theoretical Background section) and ensures best possible comparability of the results of INS and HB/FLN. Thus, this representation of $S_1(Q,\omega)$ implicitly accounts for both, vibrational density of states $g(\omega)$, and thermal population $n(\omega)$ (see eq 3). The intensity ratio between elastic and inelastic contributions is given by the Debye−Waller factor, which is completely determined by the average mean square displacement $\langle u^2 \rangle$ determined above for every temperature. As discussed above a quasielastic contribution to the INS spectra is not observed for temperatures below 100 K, so that use of eq 3 appears to be justified. Then, the elastic peak and the one-phonon functions $S_1(Q,\omega)$ for the neutron energy gain and loss sides are convoluted separately with Gaussians accounting for the energy resolution at their maxima. The energy transfer dependence of the resolution has been calculated according to Lechner[55] by taking into account the experimentally obtained elastic resolution width.

First, the 2 Å INS data were fit for a temperature of 5 K. The parameters employed are $\langle u^2 \rangle = 0.006$ Å^2 and a line shape function with a maximum at 2.3 meV as well as Gaussian and Lorentzian widths of 2 and 20 meV at their low- and high-energy transfer sides, respectively. An inspection of Figure 3 reveals that the experimental data are well-fit using these parameters at 5 K. To model the temperature dependence two factors have to be taken into account: (i) the change in the intensity ratio between elastic and inelastic contributions according to the temperature dependence of $\langle u^2 \rangle$ and (ii) the change in thermal population of vibrational levels. The fits of the 40 and 80 K data given in Figure 3 confirm that the chosen one-phonon function describes the INS data reasonably well within experimental uncertainty. The fit accounts for both temperature dependence of the intensity ratio between elastic and inelastic contributions and the subsequent thermal population of vibrational levels observed at the neutron energy gain side, respectively. Furthermore, the same set of parameters was used to reproduce the INS spectra for different scattering angles at 80 K as shown by full lines in Figure 7. The latter result provides further support for both, the line shape function employed and for the average mean square displacement $\langle u^2 \rangle$ calculated above.

The fits achieved so far can be further refined involving the 5.1 Å INS data that provide a narrower resolution width and, therefore, a better distinction of inelastic and elastic features. The 5.1 Å INS spectra shown in Figure 5 are well simulated for temperatures of 40 and 80 K. A fit of the 100 K data was not attempted because of the emerging quasielastic contribution that is not taken into account in eq 3. In summary, it can be concluded that INS data of LHC II obtained with incident neutron wavelength of 2 and 5.1 Å can be simulated with a line shape function having a maximum at 2.3 meV as well as Gaussian and Lorentzian widths of 2 and 20 meV at their low-

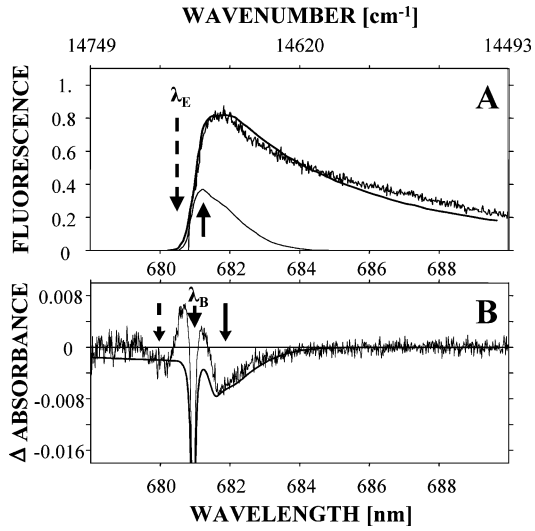

Figure 10. Frame A: experimental FLN spectrum taken from ref 34 (noisy line) obtained with $\lambda_E = 680.5$ nm. The scattered laser light has been subtracted. The fit was calculated according to eq 6 (smooth line). The contribution labeled by a full arrow is equivalent to the pseudo-phonon sideband hole of HB spectra. A wavenumber scale has been added on top of frame A for ease of inspection. Frame B: experimental HB spectrum taken from ref 29 (noisy line) obtained with $\lambda_B = 681.0$ nm and a burn fluence of 15 J/cm^2. The real- and pseudo-phonon sideband holes are indicated by full and dashed arrows, respectively.

and high-energy transfer sides, respectively. Here fits of the 5.1 Å data proved to be more sensitive to the peak position due to the higher resolution, whereas fits of the 2 Å spectra mainly established the width of the slight Lorentzian tailing toward higher energy transfers.

Simulations of HB and FLN Spectra at 5 K. To compare INS and HB/FLN, the results of refs 29 and 34 shall be briefly discussed in this section (see Figure 10). Simulations follow and refine the model used in ref 35. Hole burning experiments[29] revealed that the lowest excited (electronic) singlet state of Chl a in trimeric LHC II is characterized by a peak wavelength of $\lambda_C = 679.8 \pm 0.2$ nm and an inhomogeneous width of $\Gamma_{inh} = 80 \pm 10$ cm^{-1}. In addition, a Huang−Rhys factor $S = 0.8-0.9$ was gathered from the saturated hole depth at the low-energy wing of the absorption profile of this electronic state. The full, noisy line in frame A of Figure 10 represents the phonon wing of a 4.2 K FLN spectrum of LHC II, where the scattered laser light at the excitation wavelength of 680.5 nm has already been subtracted. It exhibits a broad and asymmetric shape with a peak at 22 cm^{-1} (∼2.7 meV). Thus, the vibrational contributions to FLN and INS spectra of LHC II are phenomenologically quite similar. Comparable results of FLN and INS experiments have already been reported for dye-doped polymers.[60] The slower tailing of the phonon wing in FLN is most likely due to a more pronounced contribution of multi-phonon processes in FLN. This is obvious since in the case of LHC II the Huang−Rhys factor S is 0.9 [29] in HB/FLN, whereas the equivalent $\langle u^2 \rangle Q^2$ values in INS are in the order of $10^{-1}-10^{-3}$ given that $\langle u^2 \rangle$ is 0.006 Å^2 at 5 K.

As discussed in the Introduction, the phonon sideband structure observed in hole burning spectra of LHC II exhibits apparent differences compared to the FLN results in both shape and peak position (see full, noisy line in frame B of Figure 10). The real-phonon sideband hole indicated by the dashed arrow interferes with the anti-hole. Therefore, the analysis should be based on the pseudo-phonon sideband hole marked by the full arrow. The peak of this sideband hole is located ∼18 cm^{-1} to higher wavelengths of the zero-phonon hole at 681 nm and has a width of only ∼25 cm^{-1}. To simulate the 4.2 K FLN and HB spectra, the values of λ_C or ω_C, Γ_{inh}, and S were varied within the range of the experimental uncertainty. The parameters ω_m, Γ_G, and Γ_L defining the one-phonon profile were assumed to be the same as those used to fit the INS spectra in the preceding section. Following this approach, the calculated FLN spectrum (see smooth line in frame A of Figure 10) was obtained according to eq 6 for $\omega_C = 14705$ cm^{-1} (680.0 nm), $\omega_E = 14695.1$ cm^{-1} (680.5 nm), $\Gamma_{inh} = 80$ cm^{-1}, and $S = 0.9$ and a one-phonon profile with $\omega_m = 18$ cm^{-1} (2.3 meV), $\Gamma_G = 16$ cm^{-1} (∼2 meV), and $\Gamma_L = 160$ cm^{-1} (∼20 meV). In general, the fit is in reasonable agreement with the experimental data. Especially, the fit accounts for the peak position and the width of the phonon wing as well as for its pronounced asymmetry.

At first glance, these data seems to be in contrast with the much narrower phonon wing of the HB data. Surprisingly, a hole burning spectrum calculated for the above data set is in complete agreement with the experimental data (see full, smooth line in frame B of Figure 10). An explanation for this effect has recently been given in a theoretical study.[35] It is based on the fact that the inhomogeneous broadening of ∼80 cm^{-1} is smaller than the width of the one-phonon profile of ∼88 cm^{-1} (∼11 meV) found above for LHC II. Briefly, in this case ($\Gamma \gtrsim \Gamma_{inh}$), the low-energy wing of the pseudo-phonon sideband hole was shown to be determined by the inhomogeneous distribution function rather than by the shape of the one-phonon profile. Consequently, the pseudo-phonon sideband hole appears to be narrower than the overall FLN spectrum. For illustration of this effect, the nonresonantly excited contribution to the FLN spectrum is shown as the lower full line in frame A of Figure 10. Although the shape of this component strongly differs from that of the overall FLN spectrum, it is very similar to the equivalent pseudo-phonon sideband hole in HB.

This leads to the striking result that both HB/FLN and INS data can be modeled using the same one-phonon profiles $l_1(\omega)$ and $S_1(\omega)$, respectively. This finding can be understood in the following way. Writing $l_1(\omega)$ explicitly according to Rebane [61] and Hayes et al.[21] as well as removing the mean frequency approximation one finds for the Stokes part of line-narrowed spectra

$$l_1(\omega) = \frac{s(\omega)}{\omega} g(\omega)[n(\omega) + 1] \tag{7}$$

where, $n = [\exp(\hbar\omega/kT) - 1]^{-1}$ is the thermal occupation number of phonons of frequency ω and $s(\omega)/\omega$ is a dimensionless expression for the frequency-dependent electron−phonon coupling strength. Especially, $2s(\omega)$ is the Stokes shift for a particular normal frequency ω of the protein system. Thus, it follows that $l_1(\omega)$ and $S_1(\omega)$ are related by the simple relation

$$l_1(\omega) = s(\omega) S_1(\omega) \tag{8}$$

where $S_1(\omega)$ represents the effective density of states weighted by the thermal population, whereas $l_1(\omega)$ contains an additional electron-vibrational coupling term. The similarity in the line shapes of $l_1(\omega)$ and $S_1(\omega)$ suggests that the electron-vibrational coupling is relatively constant across the distribution of protein normal frequencies within experimental uncertainty. This appears reasonable because a pronounced selectivity in coupling of vibrations to electronic transitions is only observed for higher-energy (localized) vibrational modes comparing Raman and Infrared spectroscopy. Given the complexity of protein (macro-) molecules such a selection cannot be expected in the frequency range of interest to this study.

Thus, it can be concluded that the low-energy protein vibrations of LHC II characterized by INS in the present study do also constitute the phonon structure observed in line-narrowing optical spectra (FLN and HB) of refs 29 and 34. The one-phonon profiles $l_1(\omega)$ and $S_1(\omega)$ used to simulate FLN/HB and INS spectra, respectively, are identical with a peak at 2.3 meV and a full width of ~11 meV under the assumption that the electron−phonon coupling term in $l_1(\omega)$ is constant in a first approximation. The latter one-phonon profile is related to the effective density of states shown in Figure 9. The shape of the one-phonon profile reported here is in good agreement but slightly narrower than that found in ref 35 (full width $\Gamma \sim 11$ vs ~13 meV in ref 35), whereas the fit quality of the FLN spectrum is somewhat better in the latter reference. This can be due to a deviation of the employed analytical line shapes from the real one-phonon profile of LHC II or due to an oversimplification of the electron−phonon coupling term in $l_1(\omega)$ in the present approach. Similarly broad one-phonon profiles were recently reported from simulations of line-narrowed spectra for the bacterial B 777[62] and LH2[36] pigment−protein complexes. Furthermore, the FLN and HB spectra of LH2 revealed a very interesting fine structure with maxima at 19 and 50 cm^{-1}.

Nevertheless, the one-phonon profile reported here for LHC II ($\Gamma \sim 11$ meV) is much broader than those found for other photosynthetic pigment−protein complexes (see, e.g., refs 18 and 21 and references therein). To find an interpretation for this wide distribution of vibrational modes in LHC II, it is instructive to refer to the work of Orecchini et al.,[42] who compared INS spectra of fully protonated and partially deuterated β-lactoglobulin. The sample deuterated mainly on external residues and side chains exhibited a shift of the vibrational peak toward higher energy transfers. It was concluded that the higher-energy vibrations are therefore localized on the protein backbone that mainly binds nonexchangeable hydrogens. In contrast to that, the lower-energy vibrations were assigned to intermolecular vibrations involving external residues and side chains, i.e., vibrations with a higher degree of delocalization and a concomitantly longer mean free path. In analogy to the latter finding, the wide distribution of protein vibrations found for LHC II most probably originates from structurally inequivalent protein domains within the LHC II trimer leading to a partial localization and, therefore, higher vibrational energy of the respective protein phonons. The protein matrix of the monomeric subunit of LHC II is formed by three membrane spanning and a forth amphipathic α-helix. These helices do not only differ in side chains and residues, but also in their lengths of 30−50 Å for the membrane-spanning α-helices;[4] that is, they are structurally inequivalent. Thus, a hypothetical but straightforward interpretation is that the low-energy vibrational peak of LHC II at about 2.3 meV corresponds to vibrations fully delocalized over the protein matrix of the LHC II monomer or trimer. In contrast to this, the slight tailing toward higher vibrational frequencies may be constituted by separate contributions from vibrations with a smaller mean free path. These vibrations might, for example, be localized on one of the different helices. The recently reported structural heterogeneity within the trimeric LHC II complex (see, e.g., ref 32) may add to the complexity of the problem. Separate, pronounced peaks in the vibrational structure were not observed in FLN/HB and INS spectra of LHC II but in the low-frequency range of FLN/HB spectra of the bacterial LH2 antenna complex.[36]

Structural heterogeneity within the LHC II complex may also offer an additional explanation for the deviations observed when fitting the 4.2 K-FLN spectrum using the one-phonon profile obtained from INS experiments (see Figure 10). The fit quality is quite good in the low-frequency range, whereas the agreement is only qualitative for higher vibrational frequencies. This can be understood in the following way. Although INS provides information on an "average" vibrational density of states of the (trimeric) LHC II complex, FLN and HB probe the electron−phonon coupling of the lowest excited electronic state of LHC II. Since this state was found to be quite highly localized on a single Chl molecule,[29] the phonon wing of the FLN spectrum shown in Figure 10 may rather reflect the fully delocalized protein vibrations as well as those partially localized in the closer proximity of the respective Chl molecule. According to Rogl and Kühlbrandt,[5] the lowest state was assigned to Chl a_2. Thus, the one-phonon profile of the lowest excited electronic state at ~680 nm might be altered in the frequency range corresponding, e.g., to vibrations localized on the more distant helix C (see Kühlbrandt et al.[4]). Such an effect would be less pronounced for higher excited electronic states that could be partly delocalized over more than one Chl molecule (see, e.g., ref 15). Regardless of a possible variation of the one-phonon profile with the local environment of a certain Chl molecule, the general agreement of the fitted FLN/HB spectra with the experimental data suggests that analysis of the INS data presented here provides a good approximation of an average one-phonon profile/ density of vibrational states for the trimeric LHC II antenna complex. However, more detailed experimental and theoretical studies, e.g., molecular dynamics simulations, are necessary to verify the conclusions given above, especially, the hypothetical assumption of structurally inequivalent protein domains as an origin of the wide distribution of protein vibrations in LHC II. Nevertheless, to the best of our knowledge the present study provides the first experimental approach to obtain $g(\omega)$ and $s(\omega)$ for a photosynthetic antenna complex by combining INS and HB/FLN spectroscopy.

Concluding Remarks

In the present study, INS experiments have been employed to study the vibrational density of states of the light-harvesting complex of photosystem II (LHC II). Two incident neutron wavelengths of 2.0 (~20 meV) and 5.1 Å (~3.2 meV) corresponding to elastic energy resolutions of $\Delta E = 0.920$ meV and $\Delta E = 0.093$ meV, respectively, were used at temperatures of 5, 40, 80 K, and 100 K.

A special preparation protocol was developed which ensured that trimeric LHC II was properly solubilized in a D_2O containing buffer solution and that the solvent scattering was significantly reduced. Solubilized LHC II and D_2O-containing buffer solution were investigated separately in order to properly subtract the contribution of the solvent.

The inelastic part of the scattering function $S(Q,\omega)$ derived for the LHC II protein resembles the well-known "Boson peak" and is characterized by a maximum at about 2.5 meV and a strongly asymmetric line shape with a slight tailing toward higher energy transfers. Analysis of the momentum transfer dependence of $S(Q,\omega)$ reveals that both the elastic and inelastic contributions to $S(Q,\omega)$ exhibit the characteristics of harmonic, vibrational protein motions. Furthermore, the effective density of vibrational states is derived from the experimental data in the low-frequency range (0−12 meV).

Simulations revealed that the INS data of LHC II presented here can be well described by a one-phonon function $S_1(\omega)$ with a maximum at 2.3 meV as well as Gaussian and Lorentzian widths of 2 and 20 meV at their low- and high-energy transfer sides, respectively. Fits of the 5.1 Å data proved to be more

sensitive to the peak position due to a narrower resolution width of 0.093 meV, whereas fits of the 2 Å spectra mainly established the width of the slight Lorentzian tailing toward higher energy transfers. The same one-phonon profile $l_1(\omega)$ can be employed to model recent results of line-narrowing optical spectroscopies (Pieper, J.; et al. *J. Phys. Chem. B* **2001**, *105*, 7115) under the reasonable assumption that the electron−phonon coupling strength is quite uniform in the investigated range of vibrational frequencies. The latter finding proves that, in principle, the vibrational density of states of LHC II found in the present study also constitutes the vibrational contribution to HB and FLN spectra.

The wide distribution of protein vibrations found for LHC II can be understood in terms of structurally inequivalent protein domains within the LHC II trimer leading to a partial localization of protein phonons. One possible interpretation is that the low-energy vibrational peak of LHC II at about 2.3 meV corresponds to vibrations fully delocalized over the protein matrix of the LHC II monomer or trimer. In contrast to this, the slight tailing toward higher vibrational frequencies may be constituted by separate contributions from vibrations with a smaller mean free path. These vibrations might, for example, be localized on one of the different α-helices forming the protein matrix of LHC II.

Acknowledgment. Financial support from Deutsche Forschungsgemeinschaft (SFB 429, TP A3) is gratefully acknowledged. We are also grateful to S. Kussin and M. Weβ (TU Berlin) for their help in sample preparation as well as to G. Steiner and B. Urban (HMI Berlin) for expert technical assistance during the neutron scattering experiments.

References and Notes

(1) Van Grondelle, R.; Dekker, J. P.; Gillbro, T.; Sundstrom, V. *Biochim. Biophys. Acta* **1994**, *1187*, 1.
(2) Renger, G. In *Concepts in Photobiology and Photomorphogenesis*; Singhal, G. S., Renger, G., Sopory, K., Irrgang, K.-D., Govindjee, Eds.; Narosa Publishing House: New Delhi, India, 1999; p 52.
(3) Paulsen, H. *Photochem. Photobiol.* **1995**, *62*, 367.
(4) Kühlbrandt, W.; Wang, D. N.; Fujiyoshi, Y. *Nature* **1994**, *367*, 614.
(5) Rogl, H.; Kühlbrandt, W. *Biochemistry* **1999**, *38*, 16214.
(6) Remelli, R.; Varotto, C.; Sandona, D.; Croce, R.; Bassi, R. *J. Biol. Chem.* **1999**, *274*, 33510.
(7) Yang, C.; Kosemund, K.; Cornet, C.; Paulsen, H. *Biochemistry* **1999**, *38*, 16205.
(8) Du, M.; Xie, X.; Mets, L.; Fleming, G. R. *J. Phys. Chem.* **1994**, *98*, 4736.
(9) Savikhin, S.; van Amerongen, H.; Kwa, S. L. S.; van Grondelle, R.; Struve, W. S. *Biophys. J.* **1994**, *66*, 1597.
(10) Bittner, T.; Irrgang, K.-D.; Renger, G.; Wasilewski, M. R. *J. Phys. Chem.* **1994**, *98*, 11821.
(11) Bittner, T.; Wiederrecht, G. P.; Irrgang, K.-D.; Renger, G.; Wasilewski, M. R. *Chem. Phys.* **1995**, *194*, 311.
(12) Connelly, J. P.; Müller, M. G.; Hucke, M.; Gatzen, G.; Mullineaux, C. W.; Ruban, A. V.; Horton, P.; Holzwarth, A. R. *J. Phys. Chem.* **1997**, *101*, 1902.
(13) Voigt, J.; Renger, T.; Schödel, R.; Schrötter, T.; Pieper, J.; Redlin, H. *Phys. Stat. Sol. (B)* **1996**, *194*, 333.
(14) Renger, T.; Voigt, J.; May, V.; Kühn, O. *J. Phys. Chem.* **1996**, *100*, 15654.
(15) Renger, T.; May, V. *Phys. Rev. Lett.* **2000**, *84*, 5228.
(16) Throughout this article the term "phonon" will be largely employed when referring to low-frequency protein vibrations (<25 meV). This is customary in studies of pigment−protein complexes in order to distinguish such modes from higher-frequency vibrational modes of the pigment molecules (60−250 meV). However, in biological systems, one is generally not dealing with phonons in a rigorous sense. Due to lack of long-range order, vibrational modes, except for long-wavelength sound waves, are expected to travel over short distances before being damped.
(17) Kühn, O.; Renger, T.; May, V.; Voigt, J.; Pullerits, T.; Sundström, V. *Trends Photochem. Photobiol.* **1997**, *4*, 213.
(18) Reddy, N. R. S.; Lyle, P. A.; Small, G. J. *Photosyn. Res.* **1992**, *31*, 167.
(19) Jankowiak, R.; Small, G. J. *Chem. Res. Toxicol.* **1991**, *4*, 256.
(20) Jankowiak, R.; Hayes, J. M.; Small, G. J. *Chem. Rev.* **1993**, *93*, 1471.
(21) Hayes, J. M.; Gillie, J. K.; Tang, D.; Small, G. J. *Biochim. Biophys. Acta* **1988**, *932*, 287.
(22) Lee, I.; Hayes, J. M.; Small, G. J. *J. Chem. Phys.* **1989**, *91* (6), 3463.
(23) Hayes, J. M.; Lyle, P. A.; Small, G. J. *J. Phys. Chem.* **1994**, *98*, 7337.
(24) Personov, R. I. In *Spectroscopy and Excitation Dynamics of Condensed Molecular Systems*; Agranovich, M., Hochstrasser, R. M., Eds.; Elsevier/North-Holland: Amsterdam, The Netherlands, 1983; p 555.
(25) Reddy, N. R. S.; van Amerongen, H.; Kwa, S. L. S.; van Grondelle, R.; Small, G. J. *J. Phys. Chem.* **1994**, *98*, 4729.
(26) Schrötter, T.; Voigt, J.; Kehrberg, G. *Photosynthetica* **1994**, *30* (4), 567.
(27) Kehrberg, G.; Voigt, J.; Schrötter, T.; Renger, G. *Biochim. Biophys. Acta* **1995**, *1231*, 147.
(28) Peterman, E. J. G.; Pullerits, T.; van Grondelle, R.; van Amerongen, H. *J. Phys. Chem. B* **1997**, *101*, 4448.
(29) Pieper, J.; Rätsep, M.; Jankowiak, R.; Irrgang, K.-D.; Voigt, J.; Renger, G.; Small, G. J. *J. Phys. Chem. A* **1999**, *103*, 2412.
(30) Tietz, C.; Jelezko, F.; Gerken, U.; Schuler, S.; Schubert, A.; Rogl, H.; Wrachtrup, J., *Biophys. J.* **2001**, *81*, 556.
(31) Jansson, S. *Biochim. Biophys. Acta* **1994**, *1184*, 1.
(32) Jansson, S. *Trends Plant Sci.* **1999**, *4*, 236.
(33) Jackowski, G. and Pielucha, K. *J. Photochem. Photobiol. B* **2001**, *64*, 45.
(34) Pieper, J.; Schödel, R.; Irrgang, K.-D.; Voigt, J.; Renger, G. *J. Phys. Chem. B* **2001**, *105*, 7115.
(35) Pieper, J.; Voigt, J.; Renger, G.; Small, G. J. *Chem. Phys. Lett.* **1999**, *310*, 296.
(36) Rätsep, M.; Freiberg, A. *Chem. Phys. Lett.* **2003**, *377*, 371.
(37) Fitter, J.; Lechner, R. E.; Dencher, N. A. *J. Phys. Chem. B* **1999**, *103*, 8036.
(38) Smith, J. C. *Q. Rev. Biophys.* **1991**, *24*, 227.
(39) Cusack, S.; Doster, W. *Biophys. J.* **1990**, *58*, 243.
(40) Doster, W.; Cusack, S.; Petry, W. *Phys. Rev. Lett.* **1990**, *65*, 1080.
(41) Ferrand, M.; Dianoux, A. J.; Petry, W.; Zaccai, G. *Proc. Natl. Acad. Sci. U.S.A.* **1993**, *90*, 9668.
(42) Frick, B.; Richter, D. *Science* **1995**, *267*, 1939.
(43) Orecchini, A.; Paciaroni, A.; Bizzarri, A. R.; Cannistraro, S. *J. Phys. Chem. B* **2001**, *105* (48), 12150.
(44) Paciaroni, A.; Orecchini, A.; Cinelli, S.; Onori, G.; Lechner, R. E.; Pieper, J. *Chem. Phys.* **2003**, *292*, 397.
(45) Paciaroni, A.; Bizzarri, A. R.; Cannistraro, S. *J. Mol. Liq.* **2000**, *84*, 3.
(46) Irrgang, K.-D.; Boekema, E. J.; Vater, J.; Renger, G. *Eur. J. Biochem.* **1988**, *178*, 209.
(47) Heukeshoven, J.; Dernick, R. *Electrophoresis* **1985**, *6*, 103.
(48) Vasil'ev, S.; Irrgang, K.-D.; Schrötter, T.; Bergmann, A.; Eichler, H.-J.; Renger, G. *Biochemistry* **1997**, *36*, 7503.
(49) Porra, R. G.; Thompson, W. A.; Kriedemann, P. E. *Biochim. Biophys. Acta* **1989**, *975*, 384.
(50) Wellburn, A. R.; Lichtenthaler, H. In *Advances in Photosynthesis Research*; Sybesma, C., Ed.; Martinus Nijhoff Publ.: The Hague, The Netherlands, 1984; Vol. II, pp 9−12.
(51) Brown, R. E.; Jarvis, K. L.; Hyland, K. J. *Anal. Biochem.* **1989**, *180*, 136.
(52) Lechner, R. E. *Physica B* **1992**, *180* & *181*, 973.
(53) Lechner, R. E. *Neutron News* **1996**, *7* (4), 9.
(54) Lechner, R. E. Melzer, R.; Fitter, J. *Physica B* **1996**, *226*, 86.
(55) Lechner, R. E. *Neutron scattering in the nineties*; IAEA: Vienna, 1985; pp 401−407.
(56) Lechner, R. E.; Riekel, C. *Neutron Scattering and Muon Spin Rotation*; Springer-Verlag: New York, 1983; p 23.
(57) Bee, M. *Quasielastic Neutron Scattering: Principles and Applications in Solid State Chemistry, Biology Materials Science*; Adam & Hilger: Philadelphia, PA, 1988.
(58) Garbers, A.; Reifarth, F.; Kurreck, J.; Renger, G.; Parak, F. *Biochemistry* **1998**, *37*, 11399.
(59) Parak, F. G. *Rep. Prog. Phys.* **2003**, *66*, 103.
(60) Kanematsu, Y.; Enomoto, M.; Nishikawa, Y.; Kushida, T.; Ahn, J. S., *J. Lumin.* **1995**, *64* (1−6), 109.
(61) Rebane, K. K. *Impurity Spectra of Solids*; Plenum Press: New York, 1970.
(62) Renger, T.; Marcus, R. A., *J. Chem. Phys.* **2001**, *116* (22), 9997.